

Isospin- and momentum-polarized orders in bilayer graphene

Zhiyu Dong, Margarita Davydova, Olumakinde Ogunnaike, Leonid Levitov
Massachusetts Institute of Technology, Cambridge, Massachusetts 02139, USA

(Dated: December 25, 2022)

Electron bands in the untwisted bilayer graphene flatten out in a transverse electric field, offering a promising platform for correlated electron physics. We predict that the spin/valley isospin magnetism, resembling that seen in moiré bands, coexists with momentum-polarized phases occurring via a “flocking transition” in momentum space in which the electron distribution is spontaneously displaced in momentum space relative to the K or K' valley centers. These phases feature unusual observables such as persistent currents in the ground state. Momentum-polarized carriers “sample” the Berry curvature of the conduction band, resulting in a unique behavior of the anomalous Hall conductivity and other effects that do not occur in previously studied systems.

I. INTRODUCTION

Narrow bands in moiré graphene[1–4] host a variety of strongly correlated phases with exotic properties that can be accessed by tuning external fields and carrier density[5–26]. These findings inspired investigations into the existence of other narrow-band systems with interesting properties. Recently, two nontwisted graphene multilayers—Bernal-stacked bilayers and ABC trilayers—have been identified[27, 28] as systems showing cascades of ordered phases resembling those seen in moiré graphene[31–35]. These systems feature electron bands with field-tunable bandgaps and dispersion that flattens out quickly as the field increases. Carriers in these bands become nearly dispersionless at large fields, forming strongly interacting systems with interesting properties[36–41, 44–46]. These developments prompted questions about new symmetry breaking types and new orders achievable in these systems.

Perhaps the most unusual aspect of these systems is that the flat band is not an isolated band, as in moiré graphene. Instead it is a flattened part of a dispersive band, with the degree of flatness and phase volume tunable by the displacement field. This behavior leads to properties distinct from those of unbiased bilayer graphene [42–44]. Here, starting from a simple framework for the interaction effects in biased bilayer graphene (BBG), we predict new order types with properties considerably richer than those of isospin-ordered phases. Electron interactions in flattened bands drive isospin (spin-valley) polarization instability and a cascade of phase transitions between states with different polarizations, resembling those known in moiré graphene[31–35]. A phase diagram for this cascade, derived below and shown in Fig. 1 a), strongly resembles the phase diagram seen experimentally[27, 29, 30].

Further, an interesting change in behavior occurs at lower densities and stronger fields, where interactions lead to an isospin-polarized Fermi sea break-up and spontaneous momentum polarization, as illustrated in Fig. 1 b). Momentum-polarized phases originate from exchange-induced “flocking” effect, wherein all carriers are shifted into one, two or three pockets at the band

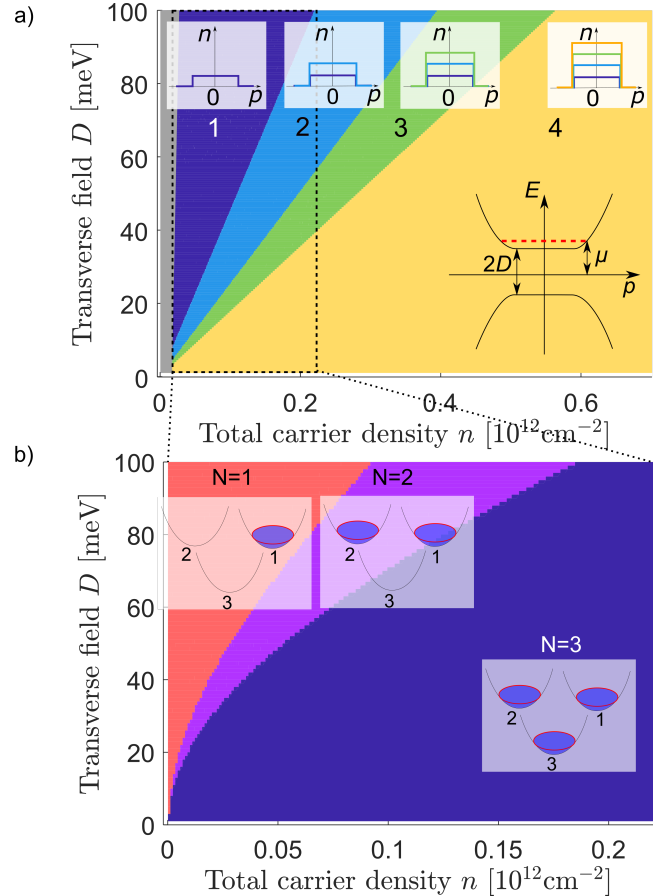


FIG. 1. a) Phase diagram for different isospin (valley and spin) orders in a lightly-doped BBG band. Carriers form Fermi seas with the degree of isospin polarization increasing with field bias. States with different numbers of isospin species, pictured in the insets, are found in the four regions of the phase diagram obtained using realistic parameters. Polarization degree varies from one layer (fully polarized) to four layers (unpolarized) [see text beneath Eq. (13)]. b) Level-two symmetry breaking occurring in a dashed box marked in a). Different orders arise due to the Fermi sea spontaneously breaking into $N = 1, 2$ or 3 pockets and shifting to different band minima [see Fig. 2].

minima produced by the trigonal warping effects. These orders develop on top of the isospin-polarized phases.

Momentum-polarized states are described phenomenologically by an effective Hamiltonian:

$$\tilde{H}(\mathbf{k}) = H(\mathbf{k}) + \mathbf{u} \cdot \mathbf{k}. \quad (1)$$

Here $H(\mathbf{k})$ is the trigonal warped Hamiltonian which we can approximate with three parabolic pockets displaced from K points, as illustrated in Fig. 2, \mathbf{u} is the order parameter that describes the polarization in momentum space. As we will see, a spatial dependent $\mathbf{u}(\mathbf{x})$ gives rise to a local persistent current and an orbital magnetization, which is allowed by the spontaneously broken time-reversal symmetry in momentum polarized phases. The persistent currents and orbital magnetization generated in this way are distinct from those familiar for the bands endowed with Berry curvature.

In addition to that, the momentum-polarized carriers “sample” the Berry curvature of the conduction band, leading to jumps and other unique signatures in the anomalous Hall effect. These effects are enhanced by the redistribution of Berry curvature throughout the conduction band resulting from its trigonal warping (see Fig. 2). An abrupt onset of a $B = 0$ Hall effect, along with anisotropy of transport due to electronic nematicity, will provide clear signatures of momentum-polarized orders.

II. AN EFFECTIVE ONE-BAND MODEL

Isospin polarization occurs when the exchange interaction between carriers in the conduction or valence band exceeds the kinetic energy. In the BBG system the kinetic energy is quenched when band dispersion is flattened by bandgap opening in the presence of a large transverse displacement field. This regime can be described by a one-band model derived by projecting the bilayer Hamiltonian to the conduction or valence band. Here we obtain this model starting from a conventional two-band model[49]:

$$H_0 = \sum_{\xi s \mathbf{p}} \Psi_{\xi s \mathbf{p}}^\dagger \left[h_0^\xi + h_t^\xi + h_a + h_{D'} \right] \Psi_{\xi s \mathbf{p}} \quad (2)$$

$$h_0^\xi = h_1(\mathbf{p})\sigma_1 + h_2(\mathbf{p})\xi\sigma_2 + D\sigma_3$$

$$h_t^\xi = v_3(p_2\xi\sigma_1 + p_1\sigma_2), \quad h_a = \frac{p^2}{2m_a}, \quad h_{D'} = -D\frac{p^2}{\tilde{p}^2}\sigma_3$$

where $\xi = K, K'$ represents valley K and K' , $s = \uparrow, \downarrow$ represents spin-up and spin-down, $\Psi_{\xi s \mathbf{p}} = (\psi_{A\xi s \mathbf{p}}, \psi_{B\xi s \mathbf{p}})^T$, $\sigma_{1,2,3}$ are the Pauli matrices acting on the valley and sublattice (layer) degrees of freedom, respectively. The quantity D is the interlayer bias generated by the transverse electric field. Here h_1 and h_2 are given by

$$h_1(\mathbf{p}) = \frac{1}{2m} (p_1^2 - p_2^2) \quad (3)$$

$$h_2(\mathbf{p}) = \frac{1}{2m} (2p_1p_2). \quad (4)$$

parameter	value	parameter	value
a	2.46 Å	v	1.1×10^6 m/s
γ_0	3.16 eV	m_a	$0.19 m_e$
γ_1	0.381 eV	m	$0.028 m_e$
γ_3	0.38 eV	v_3	1.3×10^5 m/s
D	0 – 100 meV	$\tilde{p}a_{CC}$	0.058

TABLE I. Parameters in the Hamiltonian computed based on values in Ref. [49]. The velocities are defined as $v_i = (\sqrt{3}/2)a\gamma_i$ ($i = 1$ throughout this paper). The BG band mass is defined as $m = \gamma_1/2v^2 \approx 0.028m_e$.

This model is derived under the assumption that intra- and interlayer hoppings (A1B1 and A2B1-type terms in the original Hamiltonian, which are 3.16 eV and 0.38 eV, respectively) are much larger than all other energy scales. Note that we rotated the basis by 90° with respect to Ref. [49]. Here h_t produces the trigonal warping; h_a produces the particle-hole asymmetry and $h_{D'}$ is the momentum-dependent contribution that is proportional to the displacement field with $\tilde{p} \approx 0.058/a_{CC}$ a constant (see Table I).

In this and next section, since we focus on understanding the isospin orders in $SU(4)$ -symmetric model, we ignore for now the subleading terms[49], such as trigonal warping. These terms govern subtle effects such as momentum polarization, which will be considered in Sec. IV and Sec.V.

We measure the energies in meV and the momentum is made dimensionless by multiplying by the carbon-carbon atom distance $a_{CC} = 1.46$ Å. The relevant system parameters are given in Table I.

Here, we will be interested in the regime where the field-induced bandgap $2D$ is large compared to the carrier kinetic energy (see inset in Fig. 1 a)). In this regime the upper and lower bands flatten out and effectively decouple. We therefore project the problem onto the conduction band

$$\tilde{H}_0 = \hat{P} H_0 \hat{P}, \quad (5)$$

Here, the projection operator \hat{P} is defined as

$$\hat{P} = \sum_{\xi} \frac{1}{2} \left(\frac{h_0^\xi(\mathbf{p})}{E(\mathbf{p})} + 1 \right), \quad E(\mathbf{p}) = \sqrt{D^2 + \left(\frac{p^2}{2m} \right)^2}. \quad (6)$$

This yields a one-band Hamiltonian \tilde{H}_0 of the following form:

$$\tilde{H}_0 = \sum_{i\mathbf{p}} E(\mathbf{p}) \tilde{\psi}_{i,\mathbf{p}}^\dagger \tilde{\psi}_{i,\mathbf{p}}, \quad i = K \uparrow, K \downarrow, K' \uparrow, K' \downarrow \quad (7)$$

where $\tilde{\psi}_{i,\mathbf{p}}$ is the field operator of conduction band electrons in two valleys and two spins. From now on, we write the spin indices explicitly.

Next, we modeled the electron-electron interaction as

a density-density coupling:

$$H_{int} = \frac{1}{2} \sum_{\mathbf{p}\mathbf{p}'\mathbf{q}} V_{\mathbf{q}} \psi_{\alpha\xi s, \mathbf{p}}^\dagger \psi_{\beta\xi' s', \mathbf{p}'}^\dagger \psi_{\beta\xi' s', \mathbf{p}'-\mathbf{q}} \psi_{\alpha\xi s, \mathbf{p}+\mathbf{q}}, \quad (8)$$

where i, j and α, β label the isospin (spin-valley) and sublattice degrees of freedom, respectively. At large D , the form of density-density interaction is invariant under projection:

$$\tilde{H}_{int} = \frac{1}{2} \sum_{\mathbf{p}\mathbf{p}'\mathbf{q}} V_{\mathbf{q}} \tilde{\psi}_{i, \mathbf{p}}^\dagger \tilde{\psi}_{j, \mathbf{p}'}^\dagger \tilde{\psi}_{j, \mathbf{p}'-\mathbf{q}} \tilde{\psi}_{i, \mathbf{p}+\mathbf{q}} \quad (9)$$

Similar to Eq. (7), subscripts i and j take values $K \uparrow, K \downarrow, K' \uparrow, K' \downarrow$. Here we ignore the intervalley Coulomb scattering because the interaction $V_{\mathbf{q}}$ drops as $1/q$, leading to intervalley interactions that are smaller than the intra-valley interaction by a factor of $p_F/2K$ which is as small as 0.04 at carrier density 10^{12}cm^{-2} . As a result, the Hamiltonian, Eq.(9), has an approximate isospin $SU(4)$ symmetry. We note parenthetically that at small D field, Eq. (9) is no longer a good approximation since it should include a coherence factor which depends on valley and momenta. This makes the strength of coupling between charge densities in valley K different from the coupling between charge densities in valley K and valley K' , breaking the approximate $SU(4)$ symmetry. However, this $SU(4)$ -symmetry-breaking effect is small in the regime of interest. Namely, since this coherence factors are $1 - \mathcal{O}(E_F/D)$, the difference between the coherence factor in the intervalley density-density coupling term $\psi_K^\dagger \psi_K \psi_{K'}^\dagger \psi_{K'}$ and the one in the intravalley density-density coupling term $\psi_K^\dagger \psi_K \psi_K^\dagger \psi_K$ is at most $\mathcal{O}(E_F/D)$, which is small when displacement field D is much larger than the Fermi energy E_F .

To gain insight into the parameter regime for isospin polarization occurs we use a simple constant interaction model, refining it in the subsequent analysis of momentum polarized order. The isospin order is a result of a Stoner instability arising from the exchange energy, which can be written as

$$E_{ex} = -\frac{1}{2} \sum_{i\mathbf{p}\mathbf{p}'} V_{\mathbf{q}-\mathbf{q}'} n_{i\mathbf{q}} n_{i\mathbf{q}'}, \quad n_{i\mathbf{q}} = \langle \tilde{\psi}_{i, \mathbf{q}}^\dagger \tilde{\psi}_{i, \mathbf{q}} \rangle \quad (10)$$

where i indexes isospin as in Eq. (9). Below, for simplicity, we model the interaction as a local interaction, $V_{\mathbf{q}-\mathbf{q}'} = V$.

Perhaps the closest comparison to our analysis of BBG in the literature is the early work on Stoner spin instability in BBG [38–40]. This work employed an atomic-scale short-ranged interaction, which did not allow treating valley and spin degrees of freedom on equal footing. The interaction used here, in contrast, is blind to valley and spin, leading to an approximate $SU(4)$ symmetry and a cascade of isospin orders.

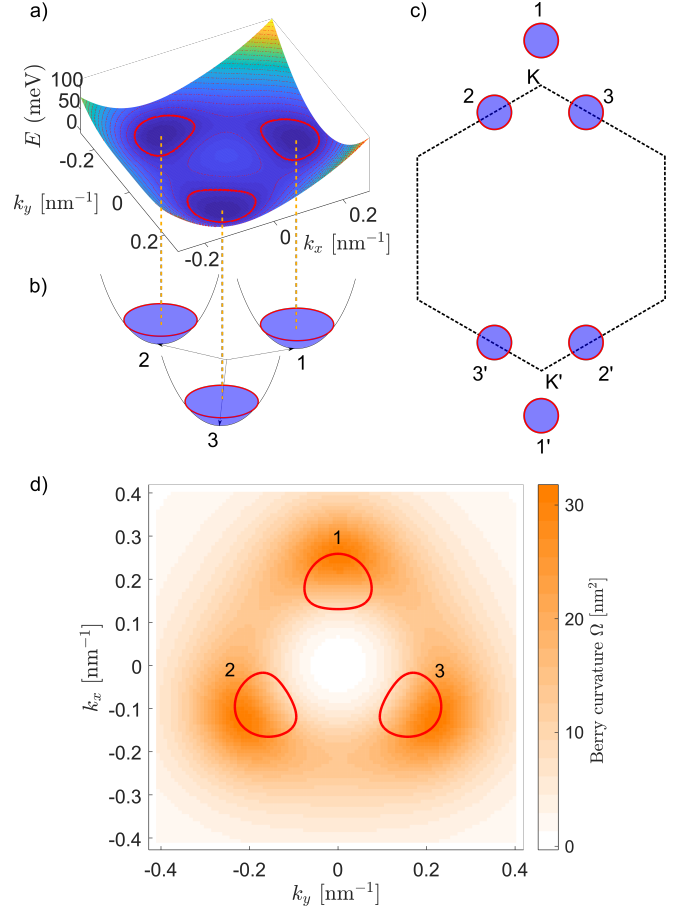


FIG. 2. a) Conduction band dispersion flattened by transverse field. Trigonal warping interaction creates three mini-valleys, at low carrier density giving rise to three electron pockets (red contours). b) A toy model for the three-pocket band structure. c) Schematic for pockets positioned near K and K' points. d) The distribution of the Berry curvature in the conduction band near K point. Parameters used: bias potential $D = 100$ meV, chemical potential $\mu = 90$ meV. The value $\mu < D$ reflects the effect of the trigonal warping.

III. BROKEN ISOSPIN $SU(4)$ SYMMETRY AND PHASE DIAGRAM

Next, we proceed to analyze the isospin polarization orders using as a framework the $SU(4)$ symmetric model introduced above. The onset of $SU(4)$ isospin polarization is determined by the Stoner criterion:

$$V\nu = 1, \quad (11)$$

with the density of states ν (per isospin species) in the conduction band,

$$\nu = \frac{m}{2\pi} \frac{\mu}{\sqrt{\mu^2 - D^2}} \approx \frac{m^2}{(2\pi)^2} \frac{D}{n}. \quad (12)$$

Here we have used the expression for the electron density in the single-electron picture, $n = \frac{m}{2\pi} \sqrt{\mu^2 - D^2}$, taking the chemical potential to lie near the bottom of the band,

$\mu \approx D$. With this, we estimate the carrier density at the onset of the Stoner instability, finding a fan of phase boundaries n vs. D for $M = 1, 2$ or 3 isospin species:

$$n_D = M \frac{Vm^2 D}{(2\pi)^2}. \quad (13)$$

While in general the mean field Stoner approach has limitations, in this case it appears to be accurate. For BBG parameters $m = 0.028m_e$ [47–49], $V = 10^3 \text{ meV nm}^2$ [see Appendix A], this simple model predicts an isospin ordering transition at carrier densities $n_D \sim 10^{12} \text{ cm}^{-2}$ for the interlayer bias $D = 100 \text{ meV}$, in excellent agreement with Ref.[27].

The mean-field phase diagram, obtained by comparing energies of partially polarized states with $M = 1, 2, 3$ and 4 isospin species found numerically, is shown in Fig. 1 a). The yellow area represents the disordered phase where all four isospin species are equally filled. Purple, light blue and green mark stability regions for isospin-ordered states. The inset in the lower right corner shows electron dispersion near charge neutrality, with the Fermi level marked by a red dashed line. The insets at the top illustrate the layer-cake structure of electron distribution in each of the phases, with the Fermi seas for different isospin species shown in different colors. The gray region near charge neutrality marks the band insulator phase with an unoccupied conduction band. The dashed rectangle marks the region of low carrier density on which the second half of this paper will focus. As we will see in Sec.IV and Sec.V, trigonal warping of the conduction band flattened by the external field D gives rise to Fermi sea breakups and level-two symmetry breaking through spontaneous momentum polarization. This behavior is summarized in the phase diagram in Fig. 1 b).

Because of the $SU(4)$ symmetry of our model, the phase diagram in Fig. 1 a) is insensitive to the order parameter orientation in the isospin space. However, in reality, small valley anisotropy in the Hamiltonian, e.g. trigonal warping or intervalley scattering, can lift the $SU(4)$ degeneracy and favor a certain orientation in isospin space. Here, rather than analyzing the competition between phases with different symmetry, we take a general symmetry approach and list all possible way of breaking the $SU(4)$ symmetry. The energetics describing this competition will be discussed elsewhere.

Our symmetry analysis benefits from the observation that the symmetry aspects of different orders and the general properties of the order parameter can be understood regardless of detailed knowledge of which order is ultimately favored. Below, we describe the possible order types, classify them through the symmetry of our problem.

For simplicity, we focus on the case of phase 1 where electrons only occupies one isospin species. Other orders can be studied in a similar manner. Table II summarizes the results for phase 1. In this case there are two possible phases, O_1^z and O_1^{xy} , describing orders with valley imbalance and intervalley coherence, respectively. These two

order types break different symmetries and have different signature observables as a result.

We arrive at this conclusion as follows. In phase 1 the order parameter is simply a projection onto the state with a given valley-spin orientation. Therefore, it takes the form of

$$O_1 = |v\rangle\langle v| \quad (14)$$

where v is an arbitrary normalized complex-valued four-component spinor in the isospin space, $|v\rangle = (\alpha_1|u_1\rangle, \alpha_2|u_2\rangle)^T$ where $|u_1\rangle, |u_2\rangle$ are arbitrary normalized two-component state vectors in the spin subspace, α_1, α_2 are positive real numbers, $\alpha_1^2 + \alpha_2^2 = 1$. Over all phases are absorbed in $|u_1\rangle$ and $|u_2\rangle$. The symmetry analysis of the Pauli matrices in valley basis (see Table II) indicates that $\tau_{1,2}$ and τ_3 transform under different irreducible representations. Thus, an order parameter containing $\tau_{1,2}$ matrices and another one containing τ_3 corresponds to different broken symmetries. Therefore, to classify orders by symmetry, we look for an order parameter, O , that contains τ_3 or $\tau_{1,2}$ matrices only, but not a mixture of τ_3 and $\tau_{1,2}$. This gives two possible types of the order parameter with distinct symmetry: $O_1^z = \frac{1}{4}(1 \pm \tau_3)(1 + \mathbf{s} \cdot \mathbf{m})$ and $O_1^{xy} = \frac{1}{4}(1 + \gamma_1\tau_1 + \gamma_2\tau_2)(1 + \mathbf{s} \cdot \mathbf{m})$. Here, \mathbf{m} is an arbitrary vector determining the spin direction, and (γ_1, γ_2) is an arbitrary normalized real-valued vector.

The order O_1^z represents a valley imbalance order, which transforms under $A_{2,\Gamma}$ and thus, features a breakdown of the mirror symmetry that swaps the two valleys. The second order parameter, O_1^{xy} , corresponds to the intervalley coherent order that transforms under $E_{\pm K}$. It breaks the three-fold rotation, reflection and translation symmetries of the original model. This aspect clearly differentiates the AB bilayer graphene from the case of ABC trilayer: in the latter, the intervalley coherent state does not break the C_3 rotation symmetry[36]. The symmetry classification of possible orders in AB bilayer graphene is summarized in Table.II.

Our symmetry analysis allows us to identify two observables that distinguish the valley imbalance and intervalley coherent orders in phase 1. These are anisotropy of conductivity and a spatial charge density wave modulation. For valley imbalance order O_1^z , neither rotation nor translation symmetry of the space group is broken, so the conductivity is isotropic and there is no spatial pattern. In comparison, for the valley coherence order O_1^{xy} , both rotation and translation symmetries are broken. The broken rotation symmetry leads to an anisotropic conductivity, whereas the broken translation symmetry leads to a spatial pattern with momentum $2K$, i.e. a Kekulé charge density wave. On a different note, the temporal symmetry can be probed by the Hall conductance. For the valley imbalance order O_1^z where time reversal symmetry is broken, the Hall conductivity is nonvanishing. In comparison, the intervalley coherent order O_1^{xy} preserves time reversal symmetry, guaranteeing a vanishing Hall conductance. These observables are summarized in the

irreps	matrices	O_1	broken symmetries	Ohmic conductivity	spatial modulation	Hall conductivity
$A_{2,\Gamma}, 1D$	τ_3	$O_1^z = P_\tau^{\pm z} P_s^{\mathbf{m}}$	mirror, time reversal	isotropic	none	nonvanishing
$E_{\pm K}, 2D$	(τ_1, τ_2)	$O_1^{xy} = P_\tau^x P_s^{\mathbf{m}}$	rotation, mirror, translation	anisotropic	Kekulé order	vanishing

TABLE II. Symmetry classification of different isospin orders. Listed are results for two real irreducible representations (irreps) of the BBG space group under which the valley-space Pauli matrices $\tau_{1,2,3}$ can transform; other irreps are not realized by isospin-polarized orders. Column 1 lists the irreps and their dimensions. In column 3, the projection operators in valley and spin space constituting the order parameter are: $P_\tau^{\pm z} = \frac{1}{2}(1 \pm \tau_3)$, $P_\tau^\gamma = \frac{1}{2}(1 + \gamma_1 \tau_1 + \gamma_2 \tau_2)$, $P_s^{\mathbf{m}} = \frac{1}{2}(1 + \mathbf{s} \cdot \mathbf{m})$, where $\gamma = (\gamma_1, \gamma_2)^T$ with real $\gamma_{1,2}$, $\mathbf{m} = (m_1, m_2, m_3)^T$ is an arbitrary three-dimensional real vector. Columns 4-7 list broken symmetries and signature observables (see text).

last three columns in Table II.

IV. MOMENTUM-POLARIZED ORDER: THE THREE-POCKET MODEL

Next, we turn to discussing momentum-polarized ordered states that are unique to BBG. These orders are triggered by Lifshits transition in which an isospin-polarized Fermi sea splits into several distinct pockets centered around the minima of the conduction band. Following this transition, exchange interactions drive symmetry breaking between different pockets through a momentum polarization instability.

It is instructive to start with a qualitative discussion of how this instability comes into play. There is an anisotropy in a realistic BBG bandstructure at small momenta due to the trigonal warping term, which is not included in the minimal description of band structure Eq. (2). This anisotropy leads to a three-pocket shape of Fermi surface in the regime of extremely low carrier density. As a result, for each isospin, instead of uniformly filling all three pockets, there are three candidate electron configurations for the ground state, in which either one, two or all three pockets are filled. Which one wins is determined by the competition between the kinetic and the exchange energy. The kinetic energy favors the configuration where all pockets are uniformly filled, whereas the exchange energy is optimized when all electrons are placed in the same pocket, since the inter-pocket exchange interaction is weaker than the intrapocket one.

To estimate of the energy scales that govern this competition, we consider the total single-particle kinetic energy for all carriers polarized in one pocket:

$$E_{\text{kin}} \sim n^2 / 2\nu_*, \quad (15)$$

where $\nu_* \sim 5 \times 10^{-5} \text{ meV}^{-1} \text{ nm}^{-2}$ is the density of states at the bottom of a single pocket, obtained using the pocket dispersion parameters estimated below. To study the pocket order, we take into account the momentum dependence of the interaction. Then the exchange energy is:

$$E_{\text{ex}} \sim -\frac{2\pi e^2}{\kappa|p|} n^2 \sim -\frac{\sqrt{\pi}}{\kappa} e^2 n^{3/2}, \quad |p| \sim \sqrt{4\pi n}, \quad (16)$$

with the characteristic momentum scale estimated from particle spacing. As a result, the exchange energy dom-

inates at sufficiently small density $n \lesssim n_* = \frac{4\pi}{\kappa^2} e^4 \nu_*^2 \sim 10^{11} \text{ cm}^{-2}$, where we have used a realistic value $D \sim 100 \text{ meV}$ and the dielectric constant $\kappa \sim 5$ similar to dielectric constant in monolayer graphene. The realistic κ values will depend on the experimental setup.

The resulting phase diagram in the small density regime is shown in Fig. 1 b). At lowest carrier density, exchange energy dominates and all electrons prefer to polarize in a single pocket. Upon carrier density increasing, the system undergoes phase transitions, first to a two-pocket configuration, and then to a three-pocket (unpolarized) phase. For illustration, in Fig. 1 b), we set the dielectric constant to be $\kappa = 3$, so that the phase diagram showcases all possible phases. The details of the phase diagram observed in experiment may vary from system to system, since the competition of pocket orders is sensitive to screening effects that depend on the experimental setup. If screening is made stronger [e.g. by a proximal gate], the pocket-ordered state will be suppressed compared to that shown in Fig. 1 b). Alternatively, if the screening is made weaker, the pocket-polarized phase will expand, taking over a larger part of the phase diagram. We note that the energy difference between the pocket polarized and unpolarized states is of the order of 0.1 meV to 1 meV per carrier, yielding a readily accessible ordering temperature scale of a few kelvin.

We end this section with detailing the procedure through which we extract the parameters k_* and m_* used in the three-pocket model by starting from the realistic BG band structure. As we only care about the band dispersion near the band minima, we model the three-pocket band structure using three isotropic parabolic bands:

$$H_\alpha(\mathbf{p}) = \frac{(\mathbf{p} - \mathbf{k}_\alpha)^2}{2m_*}, \quad \alpha = 1, 2, 3 \quad (17)$$

Here α labels the pockets, \mathbf{p}'_α s are the centers of pockets, corresponding to three minima of the conduction band:

$$\mathbf{k}_1 = k_*(0, 1), \quad \mathbf{k}_{2,3} = k_* \left(\mp \frac{\sqrt{3}}{2}, -\frac{1}{2} \right). \quad (18)$$

The values of k_* and m_* will be specified below.

In order to relate the three-pocket bandstructure represented by three parabolas to the single-particle bandstructure shown before, we first adopt a minimal model that possesses three pockets at large displacement field D .

This model has the Hamiltonian

$$H_{3-p}^{min} = \sum_{\mathbf{p}} \psi_{i\mathbf{p}}^\dagger [h_0(\mathbf{p}) + h_t(\mathbf{p}) + h_{D'}(\mathbf{p})]_{ij} \psi_{j\mathbf{p}} \quad (19)$$

Here i labels isospin, the term $h_{D'}$ is responsible for the Mexican-hat shape dispersion. We find the value of k_* by neglecting the trigonal warping term:

$$k_*(D) \approx \tilde{p} \frac{D}{\tilde{E}}, \quad \tilde{E} = \frac{\tilde{p}^2}{2m} \approx 0.2 \text{ eV}, \quad (20)$$

The trigonal warping determines the positions of the three minima of the conduction band but has a negligible effect on the radial coordinate of these minima.

The mass m_* is a parameter that we introduced in the three-pocket toy model to mimic the bottom of the conduction band from (19). The Hamiltonian Eq.(19) near one of the minimum takes the following form

$$H(\mathbf{k}_1 + \delta\mathbf{p}) = \frac{\delta p_x^2}{2m_{*\perp}} + \frac{\delta p_y^2}{2m_{*\parallel}}, \quad (21)$$

We find that the effective mass in radial direction $m_{*\parallel}$ is determined mainly by h_D , whereas the perpendicular mass $m_{*\perp}$ is only finite when we include the trigonal warping term:

$$m_{*\parallel} \approx \frac{m\tilde{E}}{4D}, \quad m_{*\perp} \approx \frac{\tilde{p}}{6v_3}. \quad (22)$$

In our three-pocket toy model Eq.(17), we set the parameter m_* as

$$m_* = \sqrt{m_{*\perp} m_{*\parallel}}. \quad (23)$$

so that the three-pocket model reproduces the density of states of the realistic band structure.

V. STONER INSTABILITY IN THE POCKET CHANNEL. PHASE DIAGRAM.

Using the three-pocket model, we proceed to analyze the instability toward momentum-polarized state and obtain a phase diagram. For clarity, we focus on the effects arising in phase 1 [see Fig.1], where the additional effects of densities in different isospin states is absent. There are three possible candidate ground states in which electrons fill up one, two or all three pockets. To determine which one of them is the true ground state, we compare their energies E_N ($N = 1, 2, 3$ is the number of occupied pockets) at the same total carrier density n . Their energies $E_N = E_K^{(N)} + E_{ex}^{(N)}$ consist of kinetic and exchange energy contributions. Using the fact that the density of states in each pocket is a constant $\nu_* = m_*/2\pi$, we can write the total kinetic energy as

$$E_K^{(N)} = \frac{N}{2\nu_*} \frac{n^2}{N^2} = \frac{\pi n^2}{Nm_*} \quad (24)$$

In order to explore the pocket polarization, we restore the momentum dependence of the interaction in the exchange part of the free energy:

$$E_{ex}^{(N)} = -\frac{1}{2} \sum_{i,j=1}^N \sum_{\mathbf{p}, \mathbf{p}'} V_{\mathbf{p}-\mathbf{p}'} n_{i\mathbf{p}} n_{j\mathbf{p}'}, \quad V_{\mathbf{p}-\mathbf{p}'} = \frac{2\pi e^2}{\kappa |\mathbf{p} - \mathbf{p}'|}, \quad (25)$$

where $n_{i\mathbf{p}}$ is the occupation number at momentum \mathbf{p} measured relative to the pocket i center. For simplicity, as in Eq.16, we use momentum-independent dielectric constant κ . When the carrier density is small, the inter-pocket exchange interactions yield a nearly momentum-independent renormalization of the energy of each electron, which justifies approximating the Fermi surfaces in the pockets by discs centered at \mathbf{k}_i . This yields an estimate for exchange energy

$$E_{ex}^{(N)} = -\sum_{i,j=1}^N \sum_{\mathbf{p}, \mathbf{p}'} \frac{1}{2} V_{\mathbf{p}-\mathbf{p}'+\mathbf{k}_{ij}} n_{\mathbf{p}} n_{\mathbf{p}'}, \quad (26)$$

$$V_{\mathbf{p}-\mathbf{p}'} = \frac{2\pi e^2}{|\mathbf{p} - \mathbf{p}'|}, \quad n_{\mathbf{p}} = 1 - \theta(|p| - p_0). \quad (27)$$

where $\mathbf{k}_{ij} = \mathbf{k}_i - \mathbf{k}_j$ are momentum differences between pocket centers, $n_{\mathbf{p}}$ is the occupation number of the state with momentum \mathbf{p} measured relative to the pocket center $n_{\mathbf{p}} = 1 - \theta(|p| - p_0)$. Here p_0 is the radius of the circular Fermi surface in each pocket

$$p_0 = \sqrt{4\pi n/N}. \quad (28)$$

With these expressions, the exchange energy can be evaluated analytically by performing the Fourier transform. Namely, perform Fourier transform:

$$V(r) = \frac{e^2}{|r|} = \int \frac{d^2 p}{(2\pi)^2} e^{i\mathbf{p} \cdot \mathbf{r}} V_{\mathbf{p}} \quad (29)$$

and

$$n(x) = \int \frac{d^2 p}{(2\pi)^2} e^{i\mathbf{p} \cdot \mathbf{r}} n_{\mathbf{p}} \quad (30)$$

Then, the exchange energy can be written as

$$\begin{aligned} E_{ex}^{(N)} &= -\frac{1}{2} \sum_{ij} \int d^2 r V(r) n(\mathbf{r})^2 e^{i\mathbf{k}_{ij} \cdot \mathbf{r}} \\ &= -\frac{1}{2} \sum_{ij} \int_0^\infty V(r) n(r)^2 2\pi J_0(r|\mathbf{k}_{ij}|) x dx \end{aligned} \quad (31)$$

Here J_0 is the Bessel function. To evaluate this quantity, we need to first work out the form of $n(r)$:

$$n(r) = \int_{|p| < p_0} \frac{dp_x dp_y}{4\pi^2} e^{ip_x r} = \int \frac{dp_x}{2\pi^2} \sqrt{p_0^2 - p_x^2} e^{ip_x r}. \quad (32)$$

Passing to polar coordinates, we have

$$\begin{aligned} n(r) &= \frac{p_0^2}{2\pi^2} \int_{-\frac{\pi}{2}}^{\frac{\pi}{2}} d\theta \cos^2 \theta e^{iz \sin \theta} \\ &= \frac{p_0^2}{8\pi} [J_2(z) + 2J_0(z) + J_{-2}(z)] = \frac{p_0^2}{4\pi} [J_2(z) + J_0(z)] \end{aligned} \quad (33)$$

where $z = rp_0$, J_0 and J_2 are Bessel functions. With these expressions, we finally arrive at

$$E_{ex}^{(N)} = -\frac{e^2 p_0^4}{16\pi} \sum_{ij} \int_0^\infty dr [J_2(rp_0) + J_0(rp_0)]^2 J_0(r|\mathbf{k}_{ij}|). \quad (34)$$

Our isotropic parabolic bands model for pockets [see Eq.(17)] is expected to be accurate when the distance k_* from the pocket centers to K point is much greater than the pocket radius p_0 . This yields an upper bound for carrier density: $n \lesssim 0.3 \times 10^{12} \text{ cm}^{-2}$, where we used the value of k_* estimated above. As Fig. 1 a) indicates, the maximal density in phase 1 always satisfies the above validity condition. We can therefore use the results in Eqs. (24),(34) to determine the phase diagram by comparing the energies of one-pocket, two-pocket and three-pocket configurations.

VI. MOMENTUM-POLARIZED PHASES: OBSERVABLES AND PHENOMENOLOGY

There are several unique observables that can be predicted for the momentum polarized phases. One surprising phenomenon that these phases display is the presence of persistent currents in the ground state, which are allowed by spontaneously-broken time reversal and inversion broken due to the transverse electric field. Such currents will not survive in a spatially uniform system bulk, yet they will show up at boundaries and interfaces. For example, they are expected to occur in the presence of spatial domains in which electrons populate different pockets. This behavior can be understood by parameterizing the momentum polarization using a position-dependent vector $\mathbf{u}(\mathbf{x})$ as in the mean-field Hamiltonian given in Eq.(1). In each domain, $\mathbf{u}(\mathbf{x})$ is a uniform vector field aligned with a certain crystal axis. For a uniform \mathbf{u} , the electric current in equilibrium equals zero since the integral over the Fermi sea of carrier velocities derived from Eq. (1) will vanish. However, at a domain wall $\mathbf{u}(\mathbf{x})$ varies in space, interpolates between different values in the domains. In this case a nonzero local current is allowed. This argument predicts a contribution to orbital magnetization first-order in spatial gradients of $\mathbf{u}(\mathbf{x})$:

$$\mathbf{m}(\mathbf{x}) = \chi \nabla \times \mathbf{u}(\mathbf{x}), \quad (35)$$

where the susceptibility χ is proportional to the Landau diamagnetic susceptibility. Here, terms such as $\nabla \cdot \mathbf{u}$

must be excluded since \mathbf{m} is an axial vector. Therefore, we expect a nonvanishing magnetization that peaks on the domain boundaries, originating from persistent currents that counter-propagate on the two sides of domain boundaries. Magnetization distribution that forms a network along domain boundaries is a directly testable signature of persistent currents.

Other interesting observables can arise from the broken crystallographic symmetries. Indeed, two possible orders of the “parent” phase, i.e. phase 1, correspond to two kinds of broken symmetries— either breaking only mirror symmetry, or breaking rotation, mirror and translation symmetries (see Table II). If phase 1 only breaks mirror symmetry, then populating one or two out of three pockets will further break the three-fold rotation symmetry without breaking the translation symmetry, leading to electron nematicity. This symmetry breaking can be observed by measuring the anisotropy in the conductivity. If, however, the parent isospin order is intervalley coherent, then the only remaining symmetry to be broken in the pocket-polarization transition is the translation symmetry. Namely, the pocket polarization on top of valley coherent states transforms the Kekulé charge density wave into an incommensurate density wave which carries momentum $\mathbf{P}_{i,j'} = 2\mathbf{K} + \mathbf{k}_i + \mathbf{k}_{j'}$, $i, j = 1, 2, 3$, $\mathbf{k}_{i'} = -\mathbf{k}_i$, see Fig. 2 c). In this case, the pocket order can be detected by imaging long-period spatial modulations.

The momentum-polarized pocket orders can also be detected by measuring the Hall conductivity. When pocket orders occur on top of the valley imbalance order O_1^z which allows a nonvanishing Hall conductivity, the Hall conductivity changes abruptly since the Berry curvature is non-uniform near K point [see Fig. 2 d)]. If pocket ordering occurs on top of O_1^{xy} isospin order, which originally respects the time reversal symmetry, enforcing a vanishing Hall conductivity, then the onset of such a momentum polarization can break the time-reversal symmetry so long as electrons populate different pockets in valleys K and K' [e.g. pocket 1 and 2' in Fig. 2 c)]. As a result, the Hall conductivity will jump from zero to some finite value at the pocket ordering transition. Therefore, regardless of the form of the parent isospin order, we always expect a discontinuous behavior in Hall conductance at the onset of pocket orders.

Another experimentally accessible signature of the Berry curvature is magnetization due to orbital currents in the ground state of the system. The magnetization can be estimated using the approach described in Refs.[50, 51], giving ~ 4 Bohr magnetons per electron for the parameters used in Fig. 2 d) [see Appendix B]. This is few times larger than the orbital magnetic moments of electrons in a Landau level, and is readily measurable.

In summary, exchange interactions in the flattened BBG bands result in a cascade of isospin-polarized orders and momentum-polarized orders. These orders are of interest for a number of reasons, in particular because they feature persistent currents and magnetization in the ground state. We stress that this phenomenon

is distinct from orbital magnetization familiar in topological bands where it arises due to Berry phase. The momentum-polarized orders, rather than merely providing additional symmetry-breaking options by extending 4 isospin species to 12 isospin and pocket species, lead to unique physical properties such as nematic order with broken time reversal, persistent currents and Hall conductivity. Momentum polarization results in abrupt

changes of the Berry curvature seen by electrons, leading to jumps in the anomalous Hall conductivity and orbital magnetization that can provide a convenient diagnostic of momentum polarization orders.

This work was supported by the Science and Technology Center for Integrated Quantum Materials, NSF Grant No. DMR1231319 and Army Research Office Grant W911NF-18-1-0116.

-
- [1] R. Bistritzer and A. H. MacDonald, Moiré bands in twisted double-layer graphene, PNAS 108, 30 (2011)
 - [2] E. J. Mele, Commensuration and interlayer coherence in twisted bilayer graphene, Phys. Rev. B 81, 161405(R) (2010)
 - [3] E. Suárez Morell, J. D. Correa, P. Vargas, M. Pacheco, and Z. Barticevic, Phys. Rev. B 82, 121407 (R) (2010)
 - [4] J. M. B. Lopes dos Santos, N. M. R. Peres, and A. H. Castro Neto, Phys. Rev. Lett. 99, 256802 (2007)
 - [5] Y. Cao, V. Fatemi, S. Fang, K. Watanabe, T. Taniguchi, E. Kaxiras, and P. Jarillo-Herrero, Nature 556, 43 (2018).
 - [6] Y. Cao, V. Fatemi, A. Demir, S. Fang, S. L. Tomarken, J. Y. Luo, J. D. Sanchez-Yamagishi, K. Watanabe, T. Taniguchi, E. Kaxiras, R. C. Ashoori, and P. Jarillo-Herrero, Nature 556, 80 (2018).
 - [7] J. Kang and O. Vafek, Strong coupling phases of partially filled twisted bilayer graphene narrow bands, Phys. Rev. Lett. 122, 246401 (2019)
 - [8] M. Xie and A. H. MacDonald, Nature of the correlated insulator states in twisted bilayer graphene, Phys. Rev. Lett. 124, 097601 (2020)
 - [9] M. Ochi, M. Koshino, and K. Kuroki, Possible correlated insulating states in magic-angle twisted bilayer graphene under strongly competing interactions, Phys. Rev. B 98, 081102(R) (2018)
 - [10] Ferromagnetic Mott state in twisted graphene bilayers at the magic angle, K. Seo, V. N. Kotov, and B. Uchoa, Phys. Rev. Lett. 122, 246402 (2019)
 - [11] F. Wu and S. Das Sarma, Ferromagnetism and superconductivity in twisted double bilayer graphene, Phys. Rev. B 101, 155149 (2020)
 - [12] F. Wu and S. Das Sarma, Collective Excitations of Quantum Anomalous Hall Ferromagnets in Twisted Bilayer Graphene, Phys. Rev. Lett. 124, 046403 (2020)
 - [13] A. L. Sharpe, E. J. Fox, A. W. Barnard, J. Finney, K. Watanabe, T. Taniguchi, M. A. Kastner, D. Goldhaber-Gordon, Emergent ferromagnetism near three-quarters filling in twisted bilayer graphene, Science, 365, 6453, 605-608 (2019)
 - [14] M. Serlin, C. L. Tschirhart, H. Polshyn, Y. Zhang, J. Zhu, K. Watanabe, T. Taniguchi, L. Balents, A. F. Young. Intrinsic quantized anomalous Hall effect in a moiré heterostructure. Science, 367, 6480 (2020)
 - [15] C. L. Tschirhart, M. Serlin, H. Polshyn, A. Shragai, Z. Xia, J. Zhu, Y. Zhang, K. Watanabe, T. Taniguchi, M. E. Huber, A. F. Young, Imaging orbital ferromagnetism in a moiré Chern insulator, Science, 372, 6548, (1323-1327), (2021).
 - [16] J. F. Dodaro, S. A. Kivelson, Y. Schattner, X. Q. Sun, and C. Wang, Phases of a phenomenological model of twisted bilayer graphene, Phys. Rev. B 98, 075154 (2018)
 - [17] S. Liu, E. Khalaf, J. Y. Lee, and A. Vishwanath, “Nematic topological semimetal and insulator in magic angle bilayer graphene at charge neutrality,” Phys. Rev. Research 3, 013033 (2021).
 - [18] A. Kerelsky, L. McGilly, D. M. Kennes, L. Xian, M. Yankowitz, S. Chen, K. Watanabe, T. Taniguchi, J. Hone, C. Dean, A. Rubio, and A. N. Pasupathy, Nature 572, 95 (2019).
 - [19] Y. Choi, J. Kemmer, Y. Peng, A. Thomson, H. Arora, R. Polski, Y. Zhang, H. Ren, J. Alicea, G. Refael, F. von Oppen, K. Watanabe, T. Taniguchi, and S. Nadj-Perge, Nat. Phys. 15, 1174 (2019).
 - [20] Y. Jiang, X. Lai, K. Watanabe, T. Taniguchi, K. Haule, J. Mao, and E. Y. Andrei, Nature 573, 91 (2019).
 - [21] Y. Cao, D. R. Legrain, J. M. Park, F. N. Yuan, K. Watanabe, T. Taniguchi, R. M. Fernandes, L. Fu, P. Jarillo-Herrero, arXiv:2004.04148 (2020).
 - [22] F. Guinea and N. R. Walet, Electrostatic effects, band distortions, and superconductivity in twisted graphene bilayers, PNAS 115 (52) 13174-13179 (2018)
 - [23] H. Isobe, N. F. Q. Yuan, and L. Fu, Unconventional Superconductivity and Density Waves in Twisted Bilayer Graphene, Phys. Rev. X 8, 041041 (2018)
 - [24] V. Kozii, H. Isobe, J. W. F. Venderbos, and L. Fu, Nematic superconductivity stabilized by density wave fluctuations: Possible application to twisted bilayer graphene, Phys. Rev. B 99, 144507 (2019)
 - [25] C. Xu and L. Balents, Topological Superconductivity in Twisted Multilayer Graphene, Phys. Rev. Lett. 121, 087001 (2018)
 - [26] Y.-P. Lin and R. M. Nandkishore, Chiral twist on the high-Tc phase diagram in moiré heterostructures, Phys. Rev. B 100, 085136 (2019)
 - [27] H. Zhou, Y. Saito, L. Cohen, W. Huynh, C. Patterson, F. Yang, T. Taniguchi, K. Watanabe, and A. F. Young, Isospin magnetism and spin-triplet superconductivity in Bernal bilayer graphene, arXiv: 2110.11317
 - [28] H. Zhou, T. Xie, A. Ghazaryan, T. Holder, J. R. Ehrets, E. M. Spanton, T. Taniguchi, K. Watanabe, E. Berg, M. Serbyn, A. F. Young. Half and quarter metals in rhombohedral trilayer graphene, arXiv:2104.00653.
 - [29] S. C. de la Barrera, S. Aronson, Z. Zheng, K. Watanabe, T. Taniguchi, Q. Ma, P. Jarillo-Herrero, R. Ashoori, Cascade of isospin phase transitions in Bernal bilayer graphene at zero magnetic field, arXiv:2110.13907
 - [30] A. M. Seiler, F. R. Geisenhof, F. Winterer, K. Watanabe, T. Taniguchi, T. Xu, F. Zhang, R. Thomas Weitz, Quantum cascade of new correlated phases in trigonally warped bilayer graphene, arXiv:2111.06413
 - [31] Y. Saito, F. Yang, J. Ge, et al. Isospin Pomeranchuk effect in twisted bilayer graphene. Nature 592, 220–224

- (2021).
- [32] U. Zondiner, A. Rozen, D. Rodan-Legrain, et al. Cascade of phase transitions and Dirac revivals in magic-angle graphene. *Nature* 582, 203–208 (2020).
 - [33] A. Rozen, J. M. Park, U. Zondiner, et al. Entropic evidence for a Pomeranchuk effect in magic-angle graphene. *Nature* 592, 214–219 (2021).
 - [34] Y. Choi, H. Kim, Y. Peng, et al. Correlation-driven topological phases in magic-angle twisted bilayer graphene. *Nature* 589, 536–541 (2021).
 - [35] A. T. Pierce, Y. Xie, J. M. Park, E. Khalaf, S. H. Lee, Y. Cao, D. E. Parker, P. R. Forrester, S. Chen, K. Watanabe, T. Taniguchi, A. Vishwanath, P. Jarillo-Herrero, A. Yacoby, Unconventional sequence of correlated Chern insulators in magic-angle twisted bilayer graphene, arXiv:2101.04123
 - [36] V. Cvetkovic, O. Vafek, Topology and symmetry breaking in ABC trilayer graphene, arXiv:1210.4923.
 - [37] Y. Lee, S. Che, J. Velasco Jr., D. Tran, J. Baima, F. Mauri, M. Calandra, M. Bockrath, C. N. Lau, Gate Tunable Magnetism and Giant Magnetoresistance in ABC-stacked Few-Layer Graphene, arXiv:1911.04450
 - [38] E. V. Castro, N. M. R. Peres, T. Stauber, and N. A. P. Silva, Low-Density Ferromagnetism in Biased Bilayer Graphene, *Phys. Rev. Lett.* 100, 186803 (2008)
 - [39] E. V. Castro, K. S. Novoselov, S. V. Morozov, N. M. R. Peres, J. M. B. Lopes dos Santos, J. Nilsson, F. Guinea, A. K. Geim and A. H. Castro Neto, Electronic properties of a biased graphene bilayer, *J. Phys.: Condens. Matter* 22 175503 (2010)
 - [40] T. Stauber, E. V. Castro, N. A. P. Silva and N. M. R. Peres, *J. Phys.: Condens. Matter* 20 335207 (2008)
 - [41] H. Min, G. Borghi, M. Polini, and A. H. MacDonald, Pseudospin magnetism in graphene, *Phys. Rev. B* 77, 041407(R) (2008)
 - [42] R. Nandkishore, L. Levitov, Flavor Symmetry and Competing Orders in Bilayer Graphene, arXiv:1002.1966v1
 - [43] V. Cvetkovic, R. E. Throckmorton, O. Vafek, Electronic multicriticality in bilayer graphene, *Phys. Rev. B* 86, 075467 (2012)
 - [44] R. E. Throckmorton and S. Das Sarma, Quantum multicriticality in bilayer graphene with a tunable energy gap *Phys. Rev. B* 90, 205407 (2014)
 - [45] J. Jung, M. Polini, and A. H. MacDonald, Persistent current states in bilayer graphene, *Phys. Rev. B* 91, 155423 (2015)
 - [46] Yang-Zhi Chou, Fengcheng Wu, Jay D. Sau, Sankar Das Sarma, Acoustic-phonon-mediated superconductivity in Bernal bilayer graphene, arXiv:2110.12303
 - [47] A. S. Mayorov, D. C. Elias, M. Mucha-Kruczynski, R. V. Gorbachev, T. Tudorovskiy, A. Zhukov, S. V. Morozov, M. I. Katsnelson, V. I. Fal'ko, A. K. Geim, and K. S. Novoselov, *Science* 333, 860 (2011).
 - [48] J. Velasco Jr., L. Jing, W. Bao, Y. Lee, P. Kratz, V. Aji, M. Bockrath, C. N. Lau, C. Varma, R. Stillwell, D. Smirnov, F. Zhang, J. Jung, and A. H. MacDonald, *Nat. Nanotechnol.* 7, 156 (2012).
 - [49] E. McCann and M. Koshino, The electronic properties of bilayer graphene, *Rep. Prog. Phys.* 76 056503 (2013)
 - [50] Di Xiao, Ming-Che Chang, and Qian Niu, Berry phase effects on electronic properties, *Rev. Mod. Phys.* 82, 1959 (2010)
 - [51] F. Aryasetiawan, K. Karlsson, Modern theory of orbital magnetic moment in solids, In: *Journal of Physics and*

Chemistry of Solids. 128, 87-108 (2019)

Appendix A: Estimating interaction strength V

In the main text, when numerically calculating the phase diagram, we are using the value of V to represent the strength of exchange interaction. Here, we provide an estimate for V values.

The interaction strength we used in our model in main text should correspond to the strength of the screened Coulomb interaction at the relevant momentum, which is Fermi momentum p_0 , i.e.

$$V = \tilde{V}_{p_0}. \quad (\text{A1})$$

Accounting for Thomas-Fermi screening, the screened Coulomb potential takes the following form

$$\tilde{V}_{p_0} = \frac{V_{p_0}}{1 + V_{p_0} \Pi_{p_0}}, \quad (\text{A2})$$

where Π_{p_0} is the polarization function at Fermi momentum. We estimate this quantity using the value of density of states at Fermi surface ν_0 . When the band is flat compared to the interaction energy, which is the case of our interest, we have

$$\nu_0 V_{p_0} \gg 1 \quad (\text{A3})$$

In this regime, the screened Coulomb interaction is approximately

$$\tilde{V}_{p_0} = \frac{1}{\nu_0}. \quad (\text{A4})$$

Therefore, we can estimate the interaction as

$$V \sim \frac{1}{\nu_0} \sim 10^3 \text{ meV nm}^2 \quad (\text{A5})$$

where we have used $\nu_0 \sim n/W \sim 10^{-3} \text{ meV nm}^{-2}$, where n is the carrier density $n \sim 10^{12} \text{ cm}^{-2}$, $W \sim 10 \text{ meV}$ is the Fermi energy measured from the band bottom at this carrier density.

Appendix B: The Berry curvature and orbital magnetization

It is straightforward to compute the Berry curvature using the Hamiltonian Eq. (19). Below, we first explain how we compute the Berry curvature in realistic BG model and obtain the result of Fig.2. We take the form of the Hamiltonian projected to conduction band in Eq. (19), and rewrite it as

$$H_{3-p}^{min} = \sum_{\mathbf{p}} \psi_{i\mathbf{p}}^\dagger \mathbf{h}(\mathbf{p}) \cdot \boldsymbol{\tau}_{ij} \psi_{j\mathbf{p}}, \quad (\text{B1})$$

$$\mathbf{h}(\mathbf{p}) \cdot \boldsymbol{\tau} = [h_0(\mathbf{p}) + h_t(\mathbf{p}) + h_{D'}(\mathbf{p})] \quad (\text{B2})$$

where $\boldsymbol{\tau} = (\tau_1, \tau_2, \tau_3)$. Then the Berry curvature is given by

$$\Omega_{\mathbf{p}} = \frac{1}{2} \frac{\mathbf{h}}{|\mathbf{h}|} \cdot \left(\frac{\partial \mathbf{h}(\mathbf{p})}{\partial p_1} \times \frac{\partial \mathbf{h}(\mathbf{p})}{\partial p_2} \right). \quad (\text{B3})$$

In main text Fig.2 we use Eq.(B3) to numerically compute the Berry curvature.

Next, we estimate the orbital magnetization which arises from Berry curvature. Below, we recap the derivation of orbital moment described in Ref. 50 and 51, and apply it to our model.

As a starting point, we consider the current flowing along the sample boundary, treating it as an anomalous current arising due to Berry's curvature and driven by the field due to spatially varying trapping potential U . This gives a current value

$$I = e \int dx n(x) v(x) \quad (\text{B4})$$

$$= e \int dx \int \frac{d^2 p}{(2\pi)^2} \Omega_{\mathbf{p}} f(\epsilon_{\mathbf{p}} - \mu + U) \frac{\partial U}{\partial x} \quad (\text{B5})$$

where x is the coordinate in the direction perpendicular to the boundary. The magnetization per unit area is therefore given by

$$M = \frac{IA}{A} = e \int_0^{\tilde{\mu}} \Omega_{FS}(\tilde{\mu} - U) dU, \quad (\text{B6})$$

$$\Omega_{FS}(E) = \int \frac{d^2 p}{(2\pi)^2} \Omega_{\mathbf{p}} f(\epsilon_{\mathbf{p}} - E) \quad (\text{B7})$$

To estimate the magnetization value, we apply Eq. (B7) to the three-pocket model used in the main text, taking $\Omega_{\mathbf{p}}$ as a constant $\Omega_{\mathbf{p}} \sim \Omega$ within the Fermi sea. This gives

$$\frac{M}{\mu_B} \approx \frac{N m_* m_e \Omega \tilde{\mu}^2}{2\pi}. \quad (\text{B8})$$

where μ_B is the Bohr magneton, m_e is the electron mass, N is the number of pockets that are filled, $\tilde{\mu}$ is Fermi level measured from the bottom of the band. We estimate M for the case shown in Fig.2, where $N = 3$, $\tilde{\mu} = 10$ meV, and $\Omega \sim 15 \text{ nm}^2$ [extracted from Fig. 2], we find

$$\frac{M}{\mu_B} \sim 4 \times 10^{-3} \text{ nm}^{-2} \sim 4n \quad (\text{B9})$$

where we used electron density $n = 10^{11} \text{ cm}^{-2}$, a value corresponding to the regime where pocket polarization is expected. This predicts a sizable orbital magnetic moment of ~ 4 Bohr magnetons per conduction electron.